International Journal of Heat and Mass Transfer 184 (2022) 122390

Contents lists available at ScienceDirect

International Journal of Heat and Mass Transfer

journal homepage: www.elsevier.com/locate/hmt

Transition from incoherent to coherent phonon thermal transport across graphene/h-BN van der Waals superlattices

Xin Wu, Qiang Han*

Department of Engineering Mechanics, School of Civil Engineering and Transportation, South China University of Technology, Guangzhou, Guangdong Province 510640, People's Republic of China

ARTICLE INFO

Article history:
Received 25 September 2021
Revised 9 November 2021
Accepted 5 December 2021

Keywords:
Graphene/h-BN heterostructure
vdW superlattice
Coherent phonon transport
Thermal conductivity

ABSTRACT

The van der Waals (vdW) superlattice, obtained by applying the concept of the periodic superlattice to two-dimensional materials using low-energy vdW physical assembly, is undoubtedly an instrumental avenue for the modulation of material properties. In the field of nanoscale thermal transport, the influence of the periodic structure of superlattice on the wave-particle phonon transport regime arouses substantial interests from the standpoint of basic physics and applied science. In the Graphene/h-BN vdW superlattice, we have found the wave-particle crossover of phonon transport, which is reflected in the transition from incoherent to coherent regime as the interface density increases. The analysis reveals that the increased thermal conductivity owing to coherent transport effects will amply compensate for the progressively increasing interface phonon scattering throughout this process. In addition, due to the stronger effects of the above two aspects, the superlattices with higher interface density are more sensitive to changes in temperature and interface coupling strength, which are manifested in the rate of change in thermal conductivity caused by their alteration, respectively. These results establish an in-depth understanding of coherent phonon transport while exploring the possibility of phonon wave-particle crossover in vdW superlattices, providing guidance for related thermal management based on phonon engineering.

1. Introduction

Since the second half of the 20th century, the novel properties brought about by emerging materials and structures have been a major theme driving the development of new technology revolutions, constantly refreshing our perceptions. Superlattices, periodic layered structures made up of two or more materials at the nanoscale, have undoubtedly become a quintessential example of performance modulation by structural design [1]. By virtue of their unique arrangement with a nanoscale period, the superlattice greatly enriches the possibilities of modulation and design of its physical properties, introducing a new paradigm for innovation in numerous fields of engineered artificial materials [2,3].

As an indispensable form of energy transfer in solid materials, phonon thermal transport, has become a pivotal issue in the miniaturization of electronic devices and the development of efficient thermoelectric-based energy conversion. Due to the presence of periodic interfaces in the superlattice, the propagation of phonons across the interfaces will behave differently as particle-like or wave-like properties, which exploits a reliable new route for the modulation of thermal conductivity. The presence of coherent phonons during thermal transport in superlattices has been predicted theoretically more than two decades ago, which also opened up the possibility of novel properties such as minimum thermal conductivity in superlattices by tuning the relevant periodic properties [4–11]. Driven by this, in addition to the first experimental observation of coherent phonon thermal transport in a GaAs/AlAs superlattice in 2012 [12], a number of thermophysical phenomena resulting from coherent phonon transport have been discovered in experimental studies of superlattice nanowires [13], metal/semiconductor superlattices [14,15] and other structures [16–19]. Notably, as a powerful tool for exploring the physical properties of materials and structures, molecular dynamics (MD) simulations have also extensively investigated coherent phonon thermal transport in Si/Ge nanowires [20] and some two-dimensional (2D) in-plane superlattices [21–25] such as graphene/hexagonal boron nitride (Gr/h-BN) superlattice ribbons. From theoretical predictions, to experimental validation, to simulation exploration, all of these demonstrate the vast promise of phonon engineering in superlattices through the design of phonon coherence to achieve thermal properties modulation.

It is no exaggeration to say that the emergence of 2D materials has ushered in a new era in materials science, not only

* Corresponding author.
E-mail address: emqhan@scut.edu.cn (Q. Han).

https://doi.org/10.1016/j.ijheatmasstransfer.2021.122390
0017-9310/

in terms of their exceptional physical and chemical properties, but also in terms of the unparalleled creativity of the abundant materials platform that has been built on their framework [26,27]. Two-dimensional van der Waals (vdW) heterostructures can be obtained by physically assembling 2D materials by means of material-integration along their out-of-plane directions through low-energy vdW interactions, which can be further designed periodically to form vdW superlattices that have had significant breakthroughs in recent experimental studies [28]. However, so far, the model systems for studies related to phonon thermal transport in vdW superlattices have basically been chosen around conventional semiconductor materials such as Si/Ge or GaAs/AlAs, and there are clearly many gaps to be filled in research related to superlattices composed of graphene (Gr) and hexagonal boron nitride (h-BN) in this field [29], which are the representatives of 2D materials.

In present work, the out-of-plane phonon thermal transport behavior of the Gr/h-BN vdW superlattice is investigated and dissected through extensive large-scale MD simulations, specifically non-equilibrium molecular dynamics (NEMD), homogeneous non-equilibrium molecular dynamics (HNEMD) and spectral heat current decomposition (SHC) methods. To begin, the same superlattice is selected as a representative structure to perform the method validation, which includes the sorting out of the simulation process under each specific method, the setting of the relevant parameters and the necessary discussion about the size effects. Then, the effect of the interface density (or period thickness) on the out-of-plane phonon thermal transport of superlattices is comprehensively investigated through the complementary advantages of the three methods, which also involves a focused discussion of the phonon transport regime. In addition, a useful discussion of the effect of temperature and interface coupling strength on their transport mechanisms has also been included. Importantly, mechanism analysis that extends to the phonon level is also conducted throughout the study to gain a deeper understanding of the phenomena while even stimulating further modulation possibilities.

2. Models and methods

2.1. Models for the Gr/h-BN vdW superlattices

Two factors should be considered in the building of Gr/h-BN vdW superlattices, namely the construction of vdW stacking structures and the periodic organization of the forming superlattice based on them. The construction of the three 2D vdW stacking structures Gr/Gr, h-BN/h-BN, and Gr/h-BN, which are localized in the superlattice, is the first item to consider. As illustrated in Fig. 1(a-b) for the cell unit, the lattice constants of Gr and h-BN with a comparable hexagonal honeycomb lattice configuration are $\alpha_{Gr} = 2.46$Åand $\alpha_{h-BN} = 2.51$Å, respectively. With such a minor difference in lattice constants, it is worth taking the average of the two, $\alpha_{SL} = 2.485$Å, as its uniform correction to reduce the complexity of the simulation. As a result, the initial structures of both will have a very modest lattice mismatch of roughly 1%, which, however, has an almost negligible effect on the thermal properties of the structures. After completing the construction of the monolayer Gr and h-BN, they can be stacked vertically along the out-of-plane direction at a spacing of 3.5Åto form the initial construction of the Gr/h-BN vdW stacking structure as shown in Fig. 1(c), which analogously leads to the Gr/Gr and h-BN/h-BN vdW structures. It should be noted that in this study only AA-type stacking with one-by-one overlapping coverage of the corresponding atoms along the out-of-plane direction is considered, due to the fact that different stacking configurations have been shown in our previous study to have no significant effect on phonon thermal transport across the Gr/h-BN vdW interface [30]. Furthermore, the lattice constants of the structure, as well as the interlayer distances, will be fine-tuned suitably based on the specific potential function throughout the thermal equilibrium process of the initial structure.

Further, Gr/h-BN vdW superlattices with different period thicknesses or interface densities can be obtained by arranging Gr and h-BN in different periodic patterns, using the three vdW stacking structures as the foundation units. Fig. 1(d) depicts a basic superlattice schematic structure in a structural schematic with a locally enlarged atomic-level perspective view to aid understanding of superlattice structural features, which ensures that complex superlattices can be represented visually and unambiguously by concise structural schematics later. Herein, the number of layers of a certain component (Gr or h-BN) within a single-period is taken as a decisive structural parameter for the superlattice and is denoted as N_p. In a superlattice, the period thickness can be calculated by N_p and the interlayer distance, which also yields the interface density used to indicate the number of Gr/h-BN vdW hetero-interfaces per unit length. Both intuitively and explicitly reflect the periodic nature of the superlattice from two distinct focuses on the characteristics of the single-period superlattice components and the hetero-interfaces, respectively. Fig. 1(e) shows the structural schematics of five Gr/h-BN vdW superlattices with a total of 24 layers, which will be used in subsequent studies related to the phonon thermal transport in the vdW superlattices, along with their associated superlattice structural parameters listed in Table1.

2.2. MD methods for the phonon thermal transport evaluation

2.2.1. The NEMD method

Phonon transport, the major heat carrier in non-metallic solids, can usually be described by Fourier's law of heat conduction, which is also the theoretical basis for the commonly used experimental methods of measuring thermal conductivity. It starts from the definition of thermal conductivity and performs the relevant statistics and calculations to obtain the thermal conductivity of the material by establishing a non-equilibrium steady state in the system, hence the term non-equilibrium molecular dynamics (NEMD) method. The Langevin thermostat, in particular, sets the local temperature, which includes heat source $T_h = T_0(1 + \Delta)$ and heat sink $T_c = T_0(1 - \Delta)$, as expressed by the average temperature T_0 and the normalized temperature difference Δ, to establish a non-equilibrium steady state with a constant temperature gradient in the system, in which the heat flux Q generated can be defined as:

$$Q = \frac{|dE/dt|}{A} \tag{1}$$

where $|dE/dt|$ represents the energy exchange rate between the heat source and the heat sink in the non-equilibrium steady state. Due to the conservation of the total energy of the system, the respective energy change rates of the heat source output and heat sink input are nearly identical during the non-equilibrium steady state. A denotes the area of the system in the direction perpendicular to the heat flux. Following that, all the effective heat transfer units in the system are defined as separate plates, with the temperature of each plate computed using the energy equalization theorem:

$$T_{slab} = \frac{1}{3Nk_B}\sum_{i=1}^{N} m_i v_i^2 \tag{2}$$

where N is the total number of atoms in the current plate, k_B is the Boltzmann constant, m_i and v_i are the mass and velocity of atom i respectively. The above-mentioned local independent temperature statistics make it possible to visually determine if the system has reached a non-equilibrium steady state and whether the temperature gradient is essentially constant. Further, the thermal

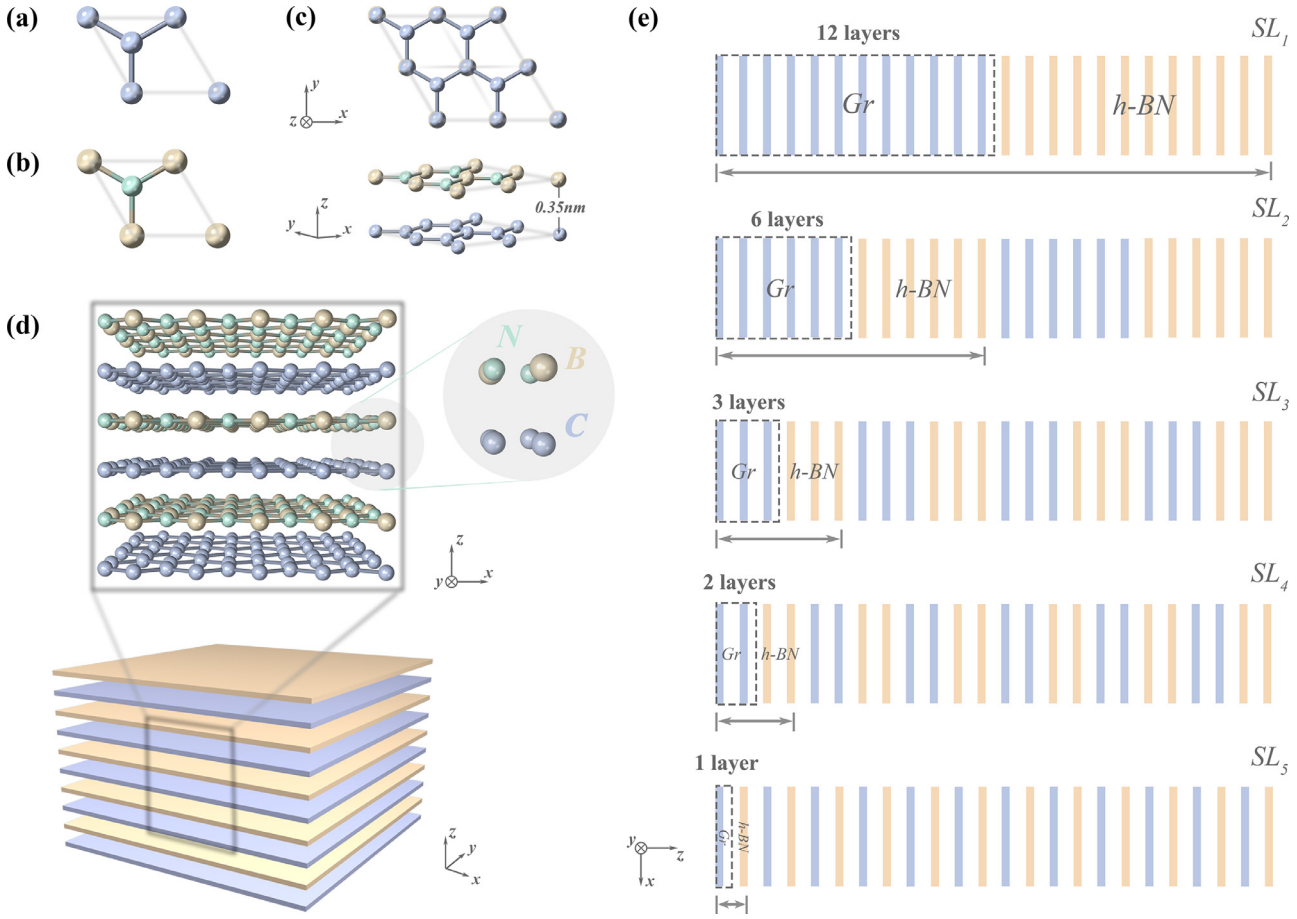

Fig. 1. The unit cell of (a) Gr and (b) h-BN. (c) Top and perspective views of the 2×2 Gr/h-BN vdW superlattice. (d) Schematic and atomic-level zoomed-in perspective view of the Gr/h-BN vdW superlattice structure with a total of 10 layers and $N_p = 1$, where all layers are spaced with 3.5Å. (e) Schematic diagram of five Gr/h-BN vdW superlattices with a total number of 24 layers. From SL_1 to SL_5, N_p is 12, 6, 3, 2, and 1, which correspond to the different period thicknesses and interface densities of these five superlattices, respectively. The part indicated by the bi-directional arrow is the single-period schematic of the corresponding superlattice. Notably here, in order to facilitate the observation of the periodic nature of the superlattice, the superlattice structural schematic focuses on the periodic arrangement of the components and omits the representation of interlayer spacing, and that the ratio of the in-plane and out-of-plane sizes, which along the x and z directions, does not represent the actual ratio.

Table 1
The relevant structural parameters of the five Gr/h-BN vdW superlattices with a total number of 24 layers, as shown in the schematic structure in Fig. 1(e).

	N_p	Number of periods	Period thickness (nm)	Interface density (nm^{-1})
SL_1	12	1	8.4	0.238
SL_2	6	2	4.2	0.476
SL_3	3	4	2.1	0.952
SL_4	2	6	1.4	1.429
SL_5	1	12	0.7	2.857

conductivity of the system along the direction of the heat flux can be obtained from the following equation:

$$\kappa = \frac{Q}{|\nabla T|} = \frac{Q}{(T_h - T_c)/L} = \frac{QL}{2T_0\Delta} \tag{3}$$

Next, some relevant technical details during the NEMD simulation for this study will be further elucidated, which will affect the accuracy and efficiency of the thermal conductivity evaluation. To begin, the system can apply the modelling setup with non-periodic or periodic boundary conditions along the thermal transport direction, where the former using fixed boundary conditions for the boundary atoms at both ends, and the latter using the common Miller-Plathe method [31]. Since there is no requirement for periodic boundary conditions in this study, as is necessary to deal with long-range electrostatic interactions, the non-periodic boundary condition will be applied to ensure the correctness of the results while avoiding the additional computational costs associated with periodic boundary conditions. In addition, the choice of thermostat used to set the local temperature may have a significant impact on MD simulations of nanoscale thermal transport. Compared to the global Nos-Hoover chain thermostat, the Langevin thermostat with its local and stochastic nature allows for more reliable and precise control of local temperatures [32,33]. Finally, unlike most earlier work, the temperature gradient is computed directly from the temperature difference between the heat source and the heat sink in Eq. (3), rather than the slope of the so-called linear region of the temperature distribution. A key issue worth noting here is that the nonlinear portion near the thermostat, whose physical origin is connected to the transport in a finite-size system [33], is wrongly ignored since this approach assumes the diffusive transport.

2.2.2. The HNEMD method

In recent years, the homogeneous non-equilibrium molecular dynamics (HNEMD) method based on non-canonical linear response theory has been continuously developed and expanded [34,35] to become an efficient method for the evaluation of the thermal conductivity by defining the thermal transport process as a mechanical analog to calculate the transport coefficient. Specifically, it initially mimics the effect of thermal gradients by applying a directed fictitious force field $\vec{F}_i^e$ to the system to generate the homogeneous heat current, where the kinetic terms that contribute little to the thermal conductivity of the solid are neglected:

$$\vec{F}_i^e = \sum_{j\neq i}\left(\frac{\partial U_j}{\partial \vec{r}_{ji}}\otimes\vec{r}_{ij}\right)\cdot\vec{F}_e \tag{4}$$

where U_j is the potential of atom j, $\vec{r}_{ij}$ and $\vec{r}_{ji}$ are the position vectors between atoms i and j, and $\vec{F}_e$ is the key vector parameter that controls the direction and magnitude of the external driving force. The total force on atom i, $\vec{F}_i^{tot}$ thus consists of both the interatomic forces $\vec{F}_i^i$ inherent in the system and the external driving forces $\vec{F}_i^e$ described above:

$$\vec{F}_i^{tot} = \vec{F}_i^i + \vec{F}_i^e = \sum_{j\neq i}\left[\frac{\partial U_i}{\partial \vec{r}_{ij}} - \frac{\partial U_j}{\partial \vec{r}_{ji}} + \left(\frac{\partial U_j}{\partial \vec{r}_{ji}}\otimes\vec{r}_{ij}\right)\cdot\vec{F}_e\right] \tag{5}$$

Further, under a general multi-body potential system, the heat flux $\vec{Q}$ is typically described as:

$$\vec{Q} = \sum_{i,j\neq i}\vec{r}_{ij}\left(\frac{\partial U_j}{\partial \vec{r}_{ji}}\cdot\vec{v}_i\right) \tag{6}$$

After applying the external driving force, the above heat flux operator is averaged over the non-equilibrium system at time t, which can be substituted by time averaging in MD, and can be expressed as:

$$\left\langle\vec{Q}(t)\right\rangle_{ne} = \left(\frac{1}{k_BT}\int_0^t\left\langle\vec{Q}(t')\otimes\vec{Q}(0)\right\rangle dt'\right)\cdot\vec{F}_e \tag{7}$$

where k_B and T are the Boltzmann constant and the system temperature, respectively, and the Green-Kubo relationship [36,37] can be combined to obtain the following running thermal conductivity results:

$$\kappa(t) = \frac{1}{k_BT^2V}\int_0^t\left\langle\vec{Q}(t')\vec{Q}(0)\right\rangle dt' = \frac{\left\langle\vec{Q}(t)\right\rangle_{ne}}{TVF_e} \tag{8}$$

where F_e denotes the modulus of the vector $\vec{F}_e$, whose dimension is the inverse length. To observe the convergence of the running thermal conductivity results better, Eq. (8) can be further rewritten by adopting the following process of cumulative averaging:

$$\kappa(t) = \frac{1}{t}\int_0^t\frac{\left\langle\vec{Q}(\tau)\right\rangle_{ne}}{TVF_e}d\tau \tag{9}$$

It should be noted that a critical issue in this method is the setting of the driving force parameter F_e, which is the basis for achieving a fully linear response with a sufficiently large signal-to-noise ratio to obtain satisfying results. The related study pointed out the following rule of thumb [35]: the linear response is fully guaranteed if the conditions $F_e\lambda \leq 1/10$ or $F_e\lambda_{\max} \leq 1$ can be satisfied, where λ and $\lambda_{\max}$ are the characteristic phonon mean free path (MFP) and the maximum phonon MFP in the system, respectively. Once the approximate upper limit has been determined, the value of F_e will be gradually reduced to ensure that the result has an appropriate signal-to-noise ratio while achieving a fully linear response. The above process is an optimization of the value of F_e based on actual problems, which is shown in detail in the Sec.3.1.2.

2.2.3. The SHC method

In the field of phonon thermal transport, understanding how specific physical quantities relate to the phonon frequency is of great significance for mechanism analysis and even for performance modulation. The spectral heat current (SHC) decomposition method, which performs spectral decomposition of the heat current in non-equilibrium MD simulations via dynamic correlation functions, has been successfully applied to two non-equilibrium MD frameworks, NEMD and HNEMD, respectively [35,38,39]. The cornerstone of the method lies in the construction of the following virial-velocity correlation function in the non-equilibrium steady state:

$$\vec{K}(t) = \sum_i\sum_{j\neq i}\left\langle\left[\vec{W}_j(0)\cdot\vec{v}_i(t)\right]\right\rangle_{ne} \tag{10}$$

where the virial force of atom j is $\vec{W}_j = \vec{v}_{ij}\frac{\partial U_j}{\partial \vec{r}_{ji}}$ and $\vec{v}_i(t)$ is the velocity of atom i at moment t. Further performing the Fourier transform and its inverse transform on it:

$$\tilde{\vec{K}}(\omega) = \int_{-\infty}^{+\infty}e^{i\omega t}\vec{K}(t)dt \quad , \quad \vec{K}(t) = \int_{-\infty}^{+\infty}e^{-i\omega t}\vec{K}(\omega)\frac{d\omega}{2\pi} \tag{11}$$

In particular, when $t = 0$, $\vec{K}(0)$ is equivalent to $\vec{Q}$ in Eq. (6), which, when combined with Eq. (11), gives:

$$\begin{aligned}\vec{Q} \equiv \vec{K}(0) &= \int_{-\infty}^{+\infty}\tilde{\vec{K}}(\omega)\frac{d\omega}{2\pi}\\ &= \int_0^{+\infty}\left[2\tilde{\vec{K}}(\omega)\right]\frac{d\omega}{2\pi}\\ &= \int_0^{+\infty}q(\omega)\frac{d\omega}{2\pi}\end{aligned} \tag{12}$$

The spectral decomposition of the heat current is thus obtained in the form of:

$$q(\omega) = 2\tilde{\vec{K}}(\omega) \tag{13}$$

Applying the above decomposition to Eq. (3) and Eq. (8) based on the NEMD method and the HNEMD method respectively, the following spectral thermal conductance $G(\omega)$ and spectral thermal conductivity $\kappa(\omega)$ are obtained:

$$G(\omega) = \frac{q(\omega)}{V\cdot(T_h - T_c)} \quad , \quad \kappa(\omega) = \frac{q(\omega)}{TVF_e} \tag{14}$$

2.2.4. Details of the MD simulations

All of the MD simulations in this study were implemented via the Graphics Processing Unit Molecular Dynamics (GPUMD) code [35,40–42], whose extremely high computational efficiency provides strong support for extensive large-scale MD simulations. More importantly, it provides generic force algorithms to implement accurate heat flux formulations applicable to multibody potential systems, avoiding the fatal errors associated with the commonly used Large-scale Atomic/Molecular Massively Parallel Simulator (LAMMPS) for thermal transport related calculations [41,43]. Furthermore, for the Gr/h-BN vdW superlattice structure in this study, the interatomic covalent interactions within the layers are described by the parametrically optimized Tersoff multibody potential [44] and the interlayer weak vdW interactions are described by the following 12-6 Lennard-Jones (L-J) potential:

$$V(r_{ij}) = 4\chi\varepsilon\left[\left(\frac{\sigma}{r_{ij}}\right)^{12} - \left(\frac{\sigma}{r_{ij}}\right)^{6}\right] \tag{15}$$

where χ denotes the interface coupling strength. ε and σ are the energy and distance constants depending on the type of atom pair combination for which vdW interactions exist, respectively, and the parameters used for the two-two pair interactions of the three

atoms B, C, and N used in this study take the values shown in Table S1 [45].

To ensure optimal system stability and energy convergence, a time step of $1fs$ was used for all simulations in this study. Also, in order to minimize the effect of boundary scattering on phonon transport, periodic boundary conditions are used in both directions within the superlattice plane. And for all simulations the following thermal equilibrium process was taken under the Berendsen thermostat-based NPT ensemble: the system was first equilibrated at 10K and zero pressure for $1ns$ (one million time steps), then the system was heated to the target temperature during the next $1ns$, and finally the NPT equilibrium was maintained at that temperature for another $1ns$. Next, depending on the specific MD method, the thermostats were switched, the system ensemble was changed, and the respective calculation and output processes were carried out, which will be described later in the corresponding section in relation to the specific model as necessary.

3. Results and discussion

3.1. Thermal conductivity across the Gr/h-BN vdW superlattice SL_5

In this section, we will take Gr/h-BN vdW superlattice SL_5 as a representative and evaluate its out-of-plane phonon thermal transport properties by the NEMD, HNEMD, and SHC methods, respectively. Through collaborative analysis, the goal is to crosscheck the results under the three methods while using their strengths to get some important insights into the phonon thermal transport across the Gr/h-BN vdW superlattice.

3.1.1. Results from NEMD

Attention needs to be paid in the NEMD method to the configuration of the structure with additional functional layers on both sides of the effective heat transfer area, that is, the fixed layers and the heat bath layers. Specifically, the outermost end is a monolayer of Gr or h-BN as the fixed layer, and inwards there are two layers of heat source layer with Gr and heat sink layer with h-BN, as shown in the inset in Fig. 2(a). After the thermal equilibrium process, the system is switched to the Langevin thermostat-controlled NVT ensemble and continues to equilibrate at a target temperature of $T_0 = 300$K for $1ns$. Next, $T_h = 330$K and $T_c = 270$K are applied to the heat source and heat sink regions via a local Langevin thermostat to achieve the non-equilibrium steady state with a constant temperature gradient. This process will last up to $10ns$, with the data required for the relevant calculations being extracted from the latter $5ns$ of the non-equilibrium steady state.

Firstly, a Gr/h-BN vdW superlattice with 20 effective heat transfer layers was used as the research object to calculate its out-of-plane thermal conductivity. As can be seen from the typical temperature profiles in the non-equilibrium steady state of Fig. 2(a), heat is constantly input from the heat source and output from the heat sink after flowing along the superlattice through the effective heat transfer area. Due to the high interface density in the superlattice SL_5, the temperature of the plate shows a relatively stable monotonic trend overall and does not show a significant discontinuous temperature distribution caused by the Kapitza thermal resistance at the Gr/h-BN vdW hetero-interface. Furthermore, energy conservation is a key indicator to ensure the stability of the simulation system, which means that the input of energy at the heat source should be approximately equal to the output at the heat sink at the same time, as is well demonstrated in Fig. 2(b).

In nanoscale phonon thermal transport, the uncertainty in phonon transport regimes (both ballistic and diffusive) brought about by the uncertain relation between the phonon MFP and the feature sizes of the system makes the discussion of the size effect along the out-of-plane direction indispensable for the adoption of non-periodic boundary conditions. Specifically, when the system feature size is less than the phonon MFP in an infinite system, the presence of the Casimir limit causes the thermal conductivity to be underestimated. For non-equilibrium MD methods, extrapolation of thermal conductivity from finite to infinite system sizes is generally achieved by the following equation [46]:

$$\begin{aligned}\frac{1}{\kappa(L)} &= \frac{1}{\kappa_0}\left(1+\frac{\lambda}{L}\right)\\ &= \frac{\lambda}{\kappa_0}\times\frac{1}{L}+\frac{1}{\kappa_0}\end{aligned} \tag{16}$$

It can be deduced from Matthiessen's rule on the left and the relation on the right as follows:

$$\frac{1}{\lambda(L)} = \frac{1}{\lambda}+\frac{1}{L}, \quad \frac{\kappa_0}{\kappa(L)} = \frac{\lambda}{\lambda(L)} \tag{17}$$

where $\kappa(L)$ denotes the thermal conductivity of a finite system of feature size L with an effective phonon MFP of $\lambda(L)$ and λ is the phonon MFP of a system of infinite size. κ_0 is the conductivity in the diffusive limit, which represents the thermal conductivity of a system with infinite feature size ($L \gg \lambda$). A slight variation of the right half of the first line in Eq. (16) reveals a linear relationship between $\kappa^{-1}(L)$ and L^{-1}, and its inverse intercept is exactly the extrapolation result of the thermal conductivity κ_0. To this end, the out-of-plane thermal conductivity was calculated by the NEMD method for five Gr/h-BN vdW superlattices with effective heat transfer layer numbers N_{total} of 10, 20, 30, 40, and 50, respectively, and two independent simulations were executed for each set of samples, as shown in Fig. 2(c). Further in Fig. 2(d), the total number of layers N_{total} is converted to the feature size L of the system by the interlayer distance and then an extrapolation of the fit as in Eq. (16) is performed to obtain $\kappa_0 \approx 4.56 Wm^{-1}K^{-1}$ with a fitness of 0.99. It is worth noting that all of the above superlattices have a cross-sectional size of $5nm \times 5nm$ and do not have to consider the in-plane size effect. In addition to the periodic boundary conditions applied in the in-plane direction which already minimize the effect of phonon scattering at the boundary, the phonon thermal transport along the out-of-plane direction is not significantly affected by the in-plane size during the NEMD simulation, as demonstrated in our previous study of similar structures [30].

3.1.2. Results from HNEMD

As the name implies, the HNEMD method is both homogeneous and non-equilibrium: the intervention of external drivers makes it non-equilibrium, while the fact that there is no real temperature gradient similar to that of the NEMD method makes it homogeneous. Since there is no need to add additional functional layers similar to those in the NEMD method, the target size superlattices are directly used as the computational structure in the HNEMD method and periodic boundary conditions are applied in all three directions. After the thermal equilibrium process, the system is switched to the Nos–Hoover thermostat-controlled NVT ensemble at a target temperature of 300K for an output stage of up to $10ns$, of which the results with good convergence in the last $5ns$ are used for post-processing calculations.

Firstly, in order to obtain a driving force parameter F_e that would allow the system to achieve a fully linear response with an appropriate signal-to-noise ratio, a Gr/h-BN vdW superlattice with an in-plane size of $5nm \times 5nm$ and a total of 20 layers was used as the base structure to perform a single simulation for six different values of F_e between $50\mu m^{-1}$ and $0.2\mu m^{-1}$. The results in Fig. 3(a) show that the parameter values of $F_e = 5\mu m^{-1}$ can meet the aforesaid requirements well, and the running thermal conductivity results produced have good convergence. However, in the case of $F_e > 5\mu m^{-1}$, the system cannot produce a fully linear response; in the case of $F_e < 5\mu m^{-1}$, the signal-to-noise ratio of the

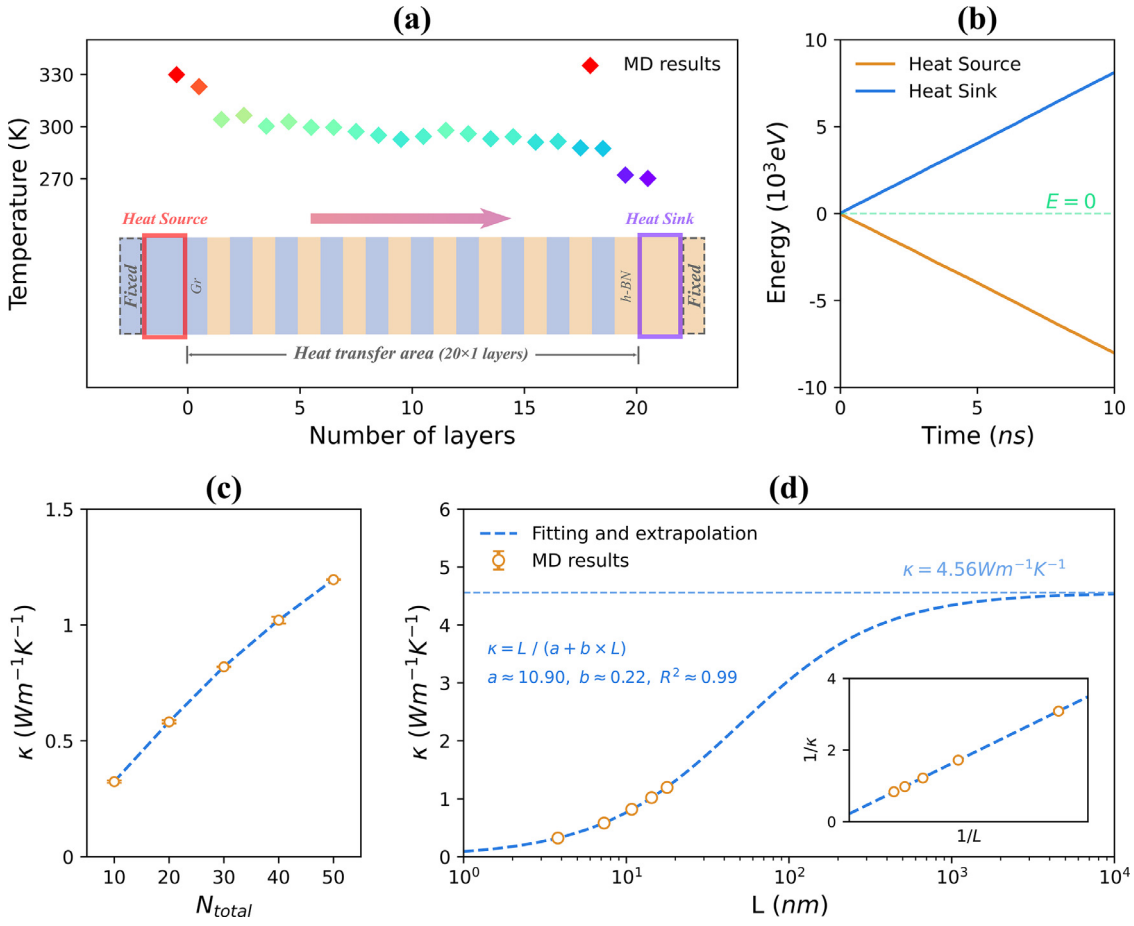

Fig. 2. (a) Typical temperature profiles of the Gr/h-BN vdW superlattice with 20 effective heat transfer layers and an in-plane size of $5nm \times 5nm$ for a temperature configuration of $T_0 = 300$K, $\Delta = 0.1$, where each MD data point represents the average temperature of the corresponding structural layer directly below it in the non-equilibrium steady state. (b) Cumulative energy values of the heat source and heat sink as a function of simulation time. Note that the two curves are almost symmetrical about the horizontal reference line $E = 0$ due to the conservation of energy in the non-equilibrium steady state. (c) The variety of thermal conductivity across the Gr/h-BN vdW superlattice with the number of effective heat transfer layers, N_{total}, under the NEMD method. (d) The thermal conductivity across the Gr/h-BN vdW superlattice as a function of the effective heat transfer area length L. The hollow circles are obtained from the MD simulations and the dashed lines are the results of fitting to them. The inset represents the inverse thermal conductivity $(1/\kappa)$ as a function of the inverse length $(1/L)$ and the two satisfy a linear relationship with a fit of up to 0.99. It should be noted that each set of MD results contains two independent simulations with error bars that are difficult to read due to their extremely small size.

results is too low to obtain accurate thermal conductivity results. Fig. 3(a) depicts the cumulative average results of the running thermal conductivity, which is an essential procedure in the data post-processing. To this end, Fig. 3(b) depicts the thermal conductivity results before and after post-processing versus simulation time for $F_e = 5\mu m^{-1}$. After the cumulative averaging of Eq. (9), the running thermal conductivity results obtained from Eq. (8) with large fluctuations become convergent and easily available. Here, the resulting average values of the running thermal conductivity converge quickly because the heat flux measured by HNEMD has a constant signal-to-noise ratio that does not decay. It enables the method to require only a limited number of independent simulations and to obtain multiple thermal conductivity results by chunking the data over a long simulation time, with the average being the final thermal conductivity result. After finalizing the values of the driving force parameter F_e and the data post-processing, two independent simulations are performed as shown in Fig. 3(c) to obtain the final thermal conductivity result of $\kappa = 4.51 \pm 0.05 Wm^{-1}K^{-1}$.

Furthermore, the effect of system size on the out-of-plane phonon thermal transport of Gr/h-BN vdW superlattices in the HNEMD method will be studied, which includes both in-plane and out-of-plane aspects. Firstly, the total number of layers of the Gr/h-BN vdW superlattice was kept at 20, and the out-of-plane thermal conductivity was calculated for six different structures with in-plane sizes of approximately $1.25nm \times 1.25nm$, $2.5nm \times 2.5nm$, $3.75nm \times 3.75nm$, $5nm \times 5nm$, $7.5nm \times 7.5nm$, and $8.75nm \times 8.75nm$, which correspond to a total number of atoms of 1200, 4800, 10800, 19200, 30000, and 48,000 respectively. The underestimating of phonon scattering owing to phonon flexural modes is one explanation for the overestimation of thermal conductivity when the in-plane sizes are small, as seen in Fig. 4(a). As the in-plane size increases, the thermal conductivity calculated in larger systems gradually decreases, converges, and achieves the desired statistical precision, which is another feature of the HNEMD method [47]. Then, the out-of-plane thermal conductivity was calculated to analyze the out-of-plane size effect for six Gr/h-BN vdW superlattices with in-plane sizes of $5nm \times 5nm$ and out-of-plane lengths of $3.5nm$, $7nm$, $10.5nm$, $14nm$, $17.5nm$, and $21nm$, respectively, with a total number of layers ranging from 10 to 60 the intervals of 10. Fig. 4(b) shows that, within reasonable error margins, the out-of-plane thermal conductivity of the superlattice with periodic boundary conditions is almost independent of the out-of-plane sizes. Therefore, under the HNEMD method, the Gr/h-BN vdW superlattice with an in-plane size of $2.5nm \times 2.5nm$ and a total of 20 layers is a desired computational structure for both computational accuracy and cost.

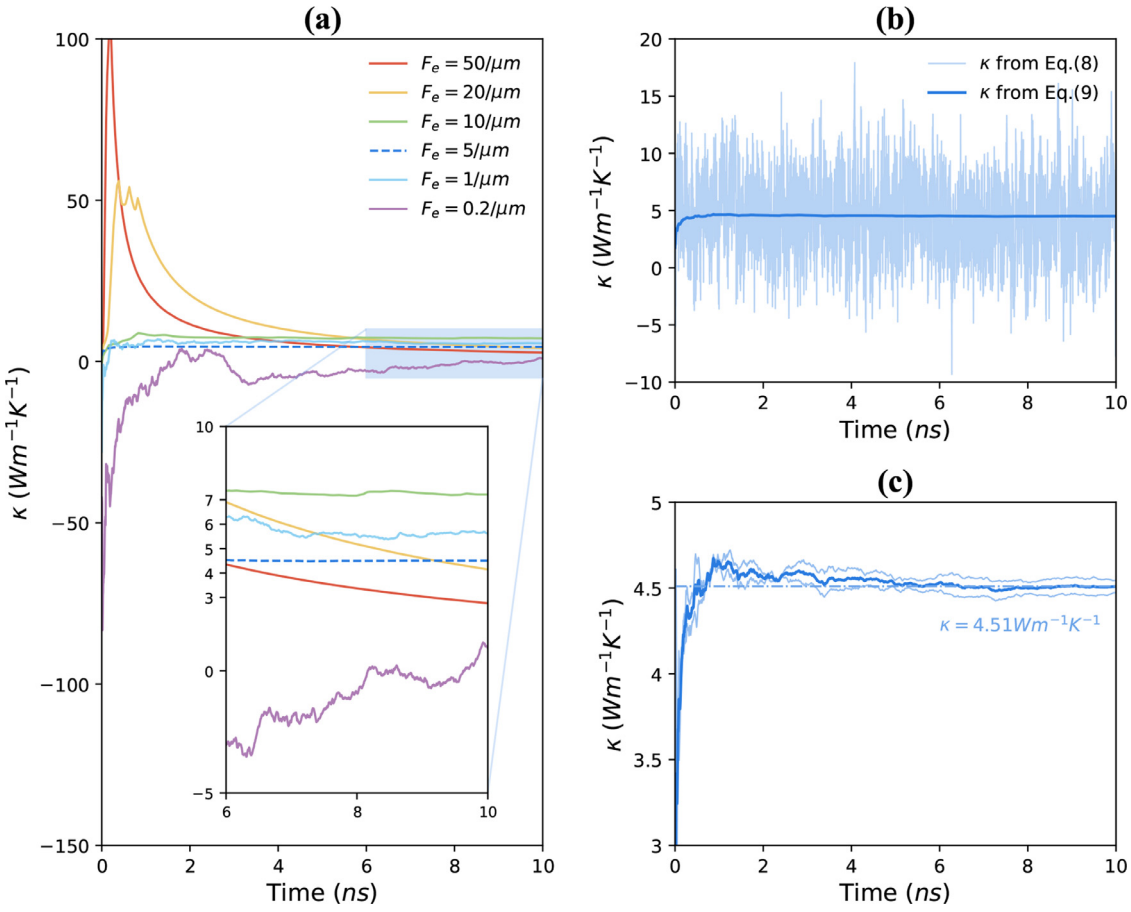

Fig. 3. The process of calculating the out-of-plane thermal conductivity of a Gr/h-BN vdW superlattice with an in-plane size of $5nm \times 5nm$ and a total number of 20 layers at 300K based on the HNEMD method and post-processing of the results. (a) The variation of running thermal conductivity with simulation time when the values of the driving force parameter F_e are $50\mu m^{-1}$, $20\mu m^{-1}$, $10\mu m^{-1}$, $5\mu m^{-1}$, $1\mu m^{-1}$, and $0.2\mu m^{-1}$, respectively. The inset zooms in on the curves for simulation time between 6ns 10ns to allow comparison of the convergence of the thermal conductivity results for different values of F_e. (b) When $F_e = 5\mu m^{-1}$, the post-processing of the thermal conductivity calculation results. The thin solid line shows the running thermal conductivity results obtained directly from Eq. (8), and the thick solid line shows the thermal conductivity results after the cumulative averaging process shown in Eq. (9) for the former, which greatly facilitates the observation of the convergence of the results. (c) Two independent simulations with different random initial velocities and their average results are presented, where the dotted line is the horizontal reference line for $\kappa = 4.51 Wm^{-1}K^{-1}$. It should be noted that the smoothness of the running thermal conductivity data results in (c) appear to differ from those in (b) due to the fact that the vertical axis of the latter takes on a range of values 15 times larger than that of the former, which inevitably hides some of the details of the curve to some extent.

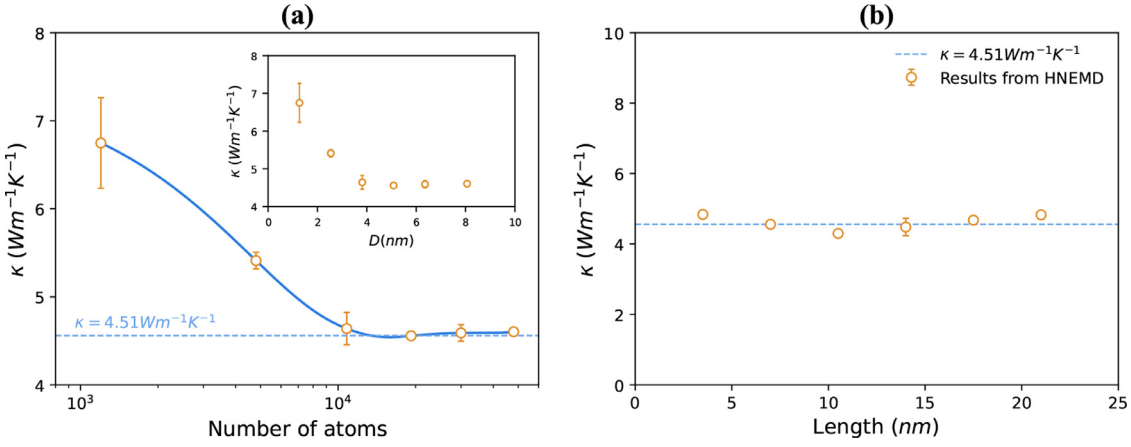

Fig. 4. (a) The out-of-plane thermal conductivity of a Gr/h-BN vdW superlattice with a total number of 20 layers as a function of the total number of atoms in the system. The total number of atoms is directly proportional to the in-plane size, which may be stated by the length D of the in-plane edge of the square in the inset when the total number of layers in the superlattice is constant. (b) Out-of-plane thermal conductivity of Gr/h-BN vdW superlattices with in-plane size of $5nm \times 5nm$ versus out-of-plane sizes (related to the total number of layers). The dashed lines in both plots indicate the horizontal reference line for $\kappa = 4.51 Wm^{-1}K^{-1}$ and the error bars are the standard deviations obtained by chunking the average results of two independent simulations.

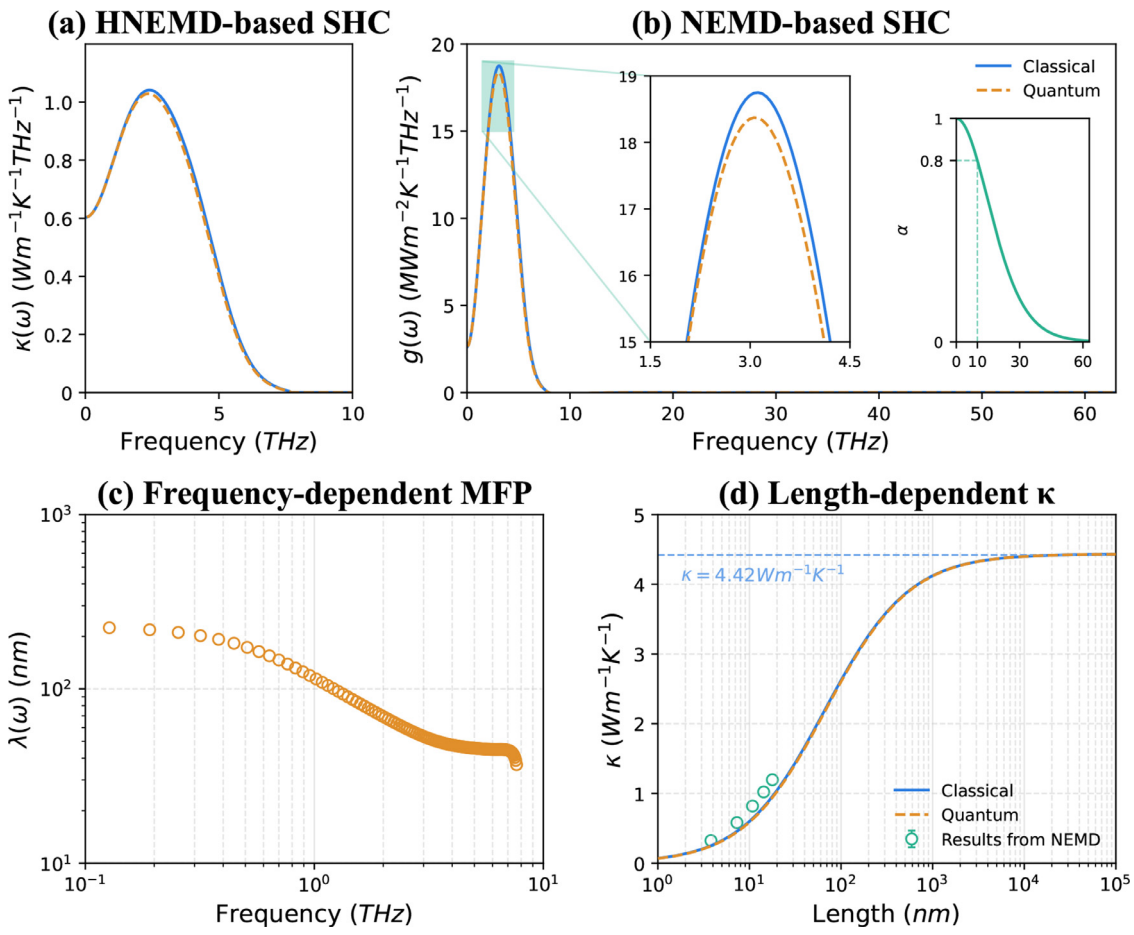

Fig. 5. Some calculation results of the out-of-plane thermal conductivity of Gr/h-BN vdW superlattices with an in-plane size of $5nm \times 5nm$ and a total number of 20 layers at the (average) temperature of 300K, based on the SHC method. The (a) spectral thermal conductivity $\kappa(\omega)$, (b) spectral ballistic thermal conductance $G(\omega)$, and (c) phonon MFP $\lambda(\omega)$ as a function of phonon frequency. The inset on the left in (b) shows an enlarged schematic of the $G(\omega)$ for the low-frequency band from $1.5THz$ to $4.5THz$ for comparing the classical results with the quantum-corrected results, and the inset on the right depicts the variation of the quantum correction factor α with phonon frequency ω at 300K. (d) Results of classical calculations of length-dependent thermal conductivity and their quantum corrections, where the dashed line indicates the horizontal reference line for $\kappa = 4.42Wm^{-1}K^{-1}$ and the hollow circle corresponds to the calculation based on the NEMD method in Section 3.1.1.

3.1.3. Results from SHC

The spectral thermal conductivity $\kappa(\omega)$ and the spectral ballistic thermal conductance $g(\omega)$ obtained by applying the heat flux that has executed the spectral decomposition to the two non-equilibrium MD simulations of HNEMD and NEMD, respectively, can help us to further obtain frequency-dependent phonon transport information, which is important for the analysis of the nature and mechanism of phonon thermal transport. The simulation procedure is identical to the HNEMD and NEMD methods because this method is based on them, as explained in Section 3.1.1 and Section 3.1.2. The complete vibrational modes of phonons cannot be fully stimulated at temperatures considerably below the Debye temperature, therefore the quantum effect cannot be ignored in this situation. Specifically, the conventional Boltzmann statistics used by phonons in MD simulations, rather of the more suitable Bose-Einstein distribution, may result in an overestimation of high-frequency phonon heat capacity and an underestimate of low-frequency phonon scattering probability. To mitigate this effect, it is necessary to introduce the following quantum correction factor α to account for possible quantum corrections [48]:

$$\alpha = \frac{x^2 e^x}{(e^x - 1)^2}, \quad x = \frac{\hbar\omega}{k_B T} \tag{18}$$

Where $\hbar$ and k_B are the Planck constant and the Boltzmann constant, respectively. T and ω are the current temperature and phonon frequency of the system, respectively. The inset on the right-hand side in Fig. 5(b) plots the relationship between the quantum correction factor α and the phonon frequency ω at 300K, which exhibits a typical distribution with a uniform low-frequency limit and a zero high-frequency limit. The necessary quantum corrections are derived by multiplying $\kappa(\omega)$ and $g(\omega)$ with α at the respective frequencies, due to the spectral decomposition of the thermal conductivity and the ballistic thermal conductance.

Herein, a Gr/h-BN vdW superlattice with in-plane size of $5nm \times 5nm$ and a total number of 20 layers was selected as the effective heat transfer object, and HNEMD- and NEMD-based SHC calculations were executed in the out-of-plane direction, respectively, and the quantum corrections shown in Eq. (18) were performed on the results, which are shown in Fig. 5(a-b). It is clear from the SHC results that the out-of-plane thermal transport in the current structure is almost entirely dominated by low-frequency phonons less than $10THz$, with a single peak at around $3THz$ as the main characteristic. By integrating $\kappa(\omega)$ and $g(\omega)$ within the frequency domain, the following classical results for thermal conductivity and ballistic thermal conductance can be obtained: $\kappa_c \approx 4.414Wm^{-1}K^{-1}$ and $G_c \approx 69.675MWm^{-2}K^{-1}$, and the following quantum corrections $\kappa_q \approx 4.325Wm^{-1}K^{-1}$ and $G_q \approx 68.066MWm^{-2}K^{-1}$. The rate of change in thermal conductivity and ballistic thermal conductance before and after quantum correction is only approximately 2.0% and 2.3%, respectively, which is even

negligible due to the uniform tend of α in the low-frequency domain. We also note that in infinite systems, the phonon MFP may be defined as the ratio of diffusive conductivity κ_0 to ballistic conductance G_0, and we extend this to the notion of frequency dependence:

$$\lambda = \frac{\kappa_0}{G_0}, \quad \lambda(\omega) \equiv \frac{\kappa_0(\omega)}{G_0(\omega)} = \frac{\kappa(\omega)}{g(\omega)} \tag{19}$$

As shown in Fig. 5(c), the previously obtained findings for $\kappa(\omega)$ and $g(\omega)$ may readily be derived to frequency-dependent phonon MFP information. At 300K, the superlattice has $\lambda_{\max} \approx 200nm$ in the out-of-plane direction, according to the results. Furthermore, the rule of thumb in Section 2.2.2 may be used to deduce the fundamental condition of $F_e \leq 5\mu m^{-1}$ for the driving force parameter in the HNEMD method, which is compatible with the parametric test findings in Fig. 3(a).

Next, the standard length-scaling formula of conductivity in Eq. (16) will be considered in terms of frequency dependence:

$$\begin{aligned} \frac{1}{\kappa(\omega, L)} &= \frac{1}{\kappa(\omega)}\left(1 + \frac{\lambda(\omega)}{L}\right) \\ &= \frac{1}{\kappa(\omega)}\left(1 + \frac{\kappa(\omega)}{g(\omega)L}\right) \end{aligned} \tag{20}$$

Further, integration of $\kappa(\omega, L)$ within the frequency domain yields the length-dependent thermal conductivity $\kappa(L)$ as shown in Fig. 5(d):

$$\kappa(L) = \int_0^\infty \kappa(\omega, L)\frac{d\omega}{2\pi} \tag{21}$$

The out-of-plane thermal conductivity converges almost completely to $\kappa \approx 4.42 Wm^{-1}K^{-1}$ when the length of the system reaches about $10\mu m$, and there is no significant difference between the results before and after the quantum correction. In addition, a comparison of the out-of-plane thermal conductivity derived by the NEMD method for the identical superlattices indicates that while there are differences, they are still in good agreement within a tolerable margin of error.

3.1.4. Comments above three results

Henceforth, we have used the NEMD, HNEMD, and SHC methods to evaluate out-of-plane thermal conductivity of the Gr/h-BN vdW superlattice and described the relevant technical details underpinning each of them. The thermal conductivity results under the three methods are $\kappa_{NEMD} \approx 4.56 Wm^{-1}K^{-1}$, $\kappa_{HNEMD} = 4.51 \pm 0.05 Wm^{-1}K^{-1}$, and $\kappa_{SHC} \approx 4.414 Wm^{-1}K^{-1}$ respectively, which show good agreement. However, compared to the NEMD method, the HNEMD method is not constrained by the out-of-plane size of the system where periodic boundary conditions are taken, and does not require the results of several structures with different out-pf-plane sizes to be repeated, which will undoubtedly result in significant savings in computational costs. Furthermore, the SHC method has successfully constructed a bridge between the NEMD and HNEMD methods and obtained frequency-dependent phonon MFP information as well as the frequency dependence of thermal conductivity, which is critical for the exploration and analysis of the phonon thermal transport mechanism. Also, due to the minor effect of the quantum effect on the out-of-plane phonon thermal transport of the superlattice in this study, they are neglected in subsequent calculations. In the next research, the HNEMD method will be utilized to calculate thermal conductivity, augmented by the SHC method to provide frequency-dependent phonon information to obtain an in-depth analysis of out-of-plane phonon thermal transport in the Gr/h-BN vdW superlattice.

3.2. Coherent phonon thermal transport in Gr/h-BN vdW superlattices

3.2.1. Transition from incoherent to coherent regime

To investigate the out-of-plane thermal transport properties of the Gr/h-BN vdW superlattices with varying period thicknesses or interface densities at 300K, the total number of layers is set to 24 and the in-plane size is set to $5nm \times 5nm$, which are illustrated in Fig. 1(e). The results obtained by the HNEMD method in Fig. 6(a) reveal that the out-of-plane thermal conductivity of the Gr/h-BN vdW superlattices tends to decrease and then increase as the interface density increases, which also implies the existence of a thermal conductivity minimum [4]. A similar interfacial density dependence of out-of-plane thermal conductivity has been found in numerous other studies of phonon thermal transport in the vdW superlattices, including theoretically, experimentally and simulatedly, as shown in Fig. 7. The mechanism underlying this dependence lies in the phonon coherence transport, as illustrated in the inset of Fig. 7: when the interface density is low, phonon transport is incoherent and exhibits a particle-like state; as the interface density increases, phonons enter a coherent regime and exhibit a wave-like state; for clarity, a short transition regime is defined between the two states, with a thermal conductivity of minimum. By comparison, the Gr/h-BN vdW superlattice in this work still has the least $\kappa_{\min}$ of all these related vdW superlattices in Fig. 7, which provides some benefits for its relevant applications in the thermal field.

In order to verify the coherence of phonon transport in the Gr/h-BN vdW superlattice, calculations of the thermal conductivity of the random superlattice are given in the next. Herein, the Gr/h-BN random vdW superlattice [49] refers to a vdW structure formed by alternating Gr and h-BN with random thicknesses for a given Gr/h-BN hetero-interface density. It is considered that superlattices with the same total number of layers and the same number of Gr/h-BN hetero-interfaces have the same interfacial density, which is adequately adapted to the structural characteristics of random superlattices. The difference between a random superlattice and a periodic superlattice (all superlattices in the text denote periodic superlattices) is whether all the components have the same thickness, and together they form an ideal pair of systems for distinguishing between coherent and incoherent phonon thermal transport. Specifically, the single-period component of the superlattice SL_5 is a monolayer of Gr or h-BN that is not continuously divisible in the out-of-plane direction. Furthermore, its not difficult to understand that this leads it has the maximum interface density so that it has no more random superlattice variants in this case. Then, for each of the four superlattices $SL_1 \sim SL_4$, five distinct random superlattices were configured at their respective interface densities, and their out-of-plane thermal conductivities were computed, the exact architectures of which are presented in Fig.S1. To begin, the thermal conductivity of the random and periodic superlattices are similar during the incoherent transport and transition regimes, which are collectively referred to as the non-coherent transport regime, but they show significant differences and exhibit opposite trends during the coherent transport regime. In the non-coherent transport regime, periodic and random superlattices with the same interfacial density should have approximately the same phonon scattering rate, which is the fundamental reason why the thermal conductivity results for both are almost identical. However, in the coherent transport regime, the coherent phonons in the random superlattice are subject to localization and thus their contribution to the thermal conductivity is neglected. As a result, the contribution of incoherent phonons can be almost entirely represented by the random superlattice thermal conductivity results in the coherent transport regime, whereas the contribution of coherent phonons is represented by the difference between the periodic superlattice and the random superlattice thermal conductivity. As the interface density increases, the phonon scattering rate

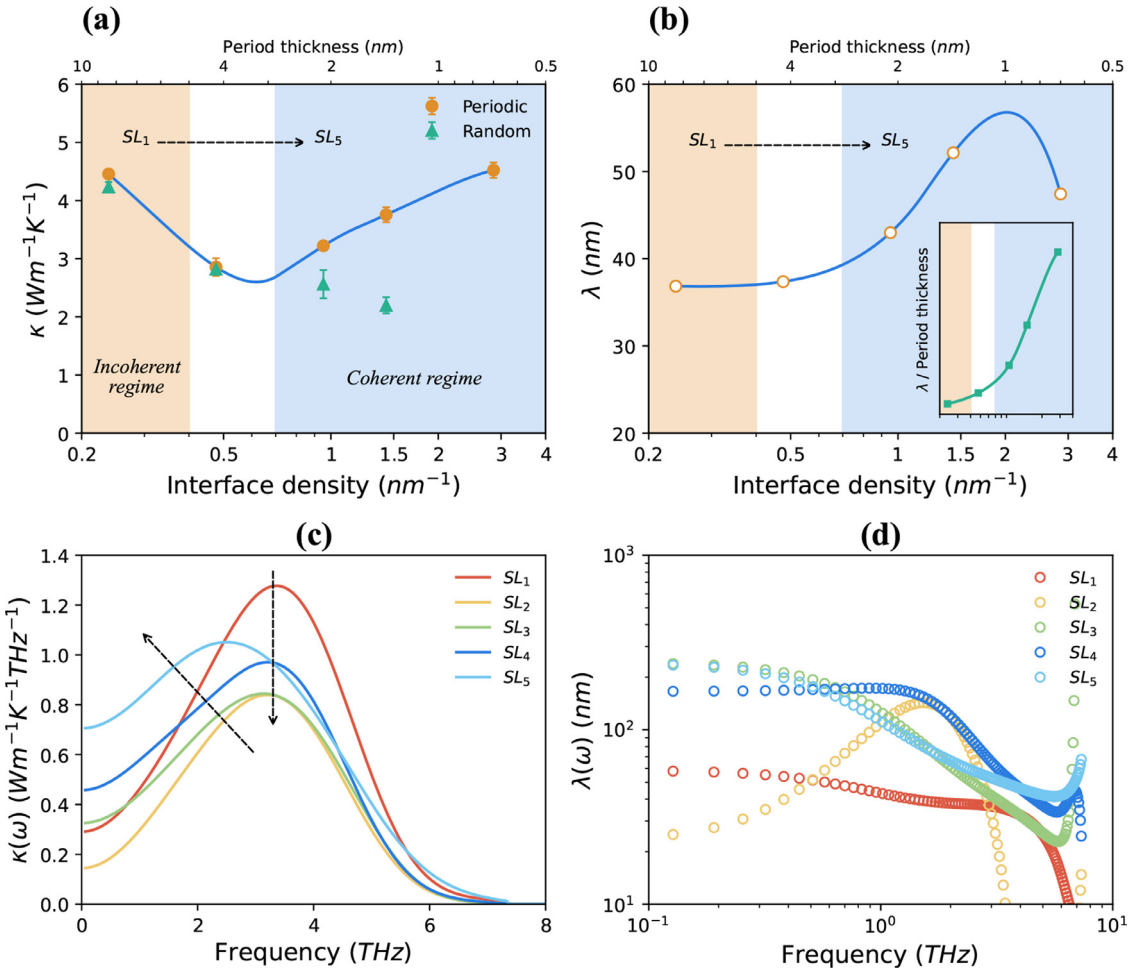

Fig. 6. Some results of the out-of-plane phonon thermal transport evaluation of Gr/h-BN vdW superlattices SL_1~SL_5 with five different interfacial densities at a total of 24 layers at 300K, whose structures are illustrated in Fig. 1(e). (a) The out-of-plane thermal conductivity calculated by the HNEMD method as a function of the interfacial density. The green triangular data denotes the calculated thermal conductivity of the random superlattice representing the incoherent phonon contribution. (b) The phonon MFP (λ) of the superlattices as a function of the interfacial density. The inset shows the ratio of the superlattice phonon MFP to its period thickness as a function of its interface density, which intuitively reflects the relationship between the superlattice phonon MFP and its periodic thickness under different interface densities. (c) Spectral thermal conductivity $\kappa(\omega)$ and (d) spectral phonon MFP $\lambda(\omega)$ results based on the SHC method, reflecting the five superlattice frequency correlations mentioned above. The black dashed arrow in (c) is the indicator of the corresponding curve for the superlattice (from SL_1 to SL_5) as the density of the interface increases. (For interpretation of the references to colour in this figure legend, the reader is referred to the web version of this article.)

will also increase, which leads to a monotonically decreasing trend in the incoherent phonon thermal conductivity represented by the random superlattice. During this process, the contribution of coherent phonons to the thermal conductivity boosts gradually from nothing, especially entering the coherent transport regime. With the combined contribution of coherent and incoherent phonons to the thermal conductivity as stated above, it is the Gr/h-BN vdW superlattice out-of-plane thermal conductivity that shows a decreasing and then increasing trend with increasing interfacial density.

Next, in order to gain further insight into the transformation of the out-of-plane phonon transport regimes in the Gr/h-BN vdW superlattice from a phonon perspective and to clarify the mechanism, the frequency-dependent spectral thermal conductivity $\kappa(\omega)$ was calculated by the SHC method, and the results are shown in Fig. 6(c). The out-of-plane thermal conductivity of the five superlattices with varying interfacial densities almost exclusively from the contribution of long-wavelength phonons at low-frequencies below $8THz$. In the process of phonon transport across the superlattice from the incoherent regime (SL_1) to the transition regime (SL_2), $\kappa(\omega)$ shows a constant position and a dramatic drop in peak due to the increase of the interface density without the participation of coherent phonons. As the interface density increases further, the phonon transport enters the coherent regime (SL_3, SL_4, and SL_5), and $\kappa(\omega)$ increases in peak with a significant transverse shift towards lower frequencies. This is due to the fact that as the interface density increases further, the reduced period thickness allows more and more low-frequency long-wavelength phonons to be involved in the coherent transport process.

Then, the phonon MFP-related information of the superlattice will be used to acquire quantitative insight into the foregoing findings as shown in Fig. 6(b, d). Since the phonon transport mechanism is determined by the relative comparison between its MFP and the length it spans, the ratio of the phonon MFP to the current superlattice period thickness is in turn used as the dependent variable to plot the inset in Fig. 6(b). In the coherent phonon transport regime, the ratio of phonon MFP to current superlattice period thickness increases monotonically with increasing interface density, implying that phonon transport will become increasingly coherent, resulting in monotonically rising thermal conductivity. However, it is worth noting that, as shown in Fig. 6(c), the effect of phonon scattering rate on the thermal conductivity due to changes in the interface density dominates in the incoherent phonon transport regime, unlike in the coherent transport regime where the degree of phonon transport coherence dominates. This also explains

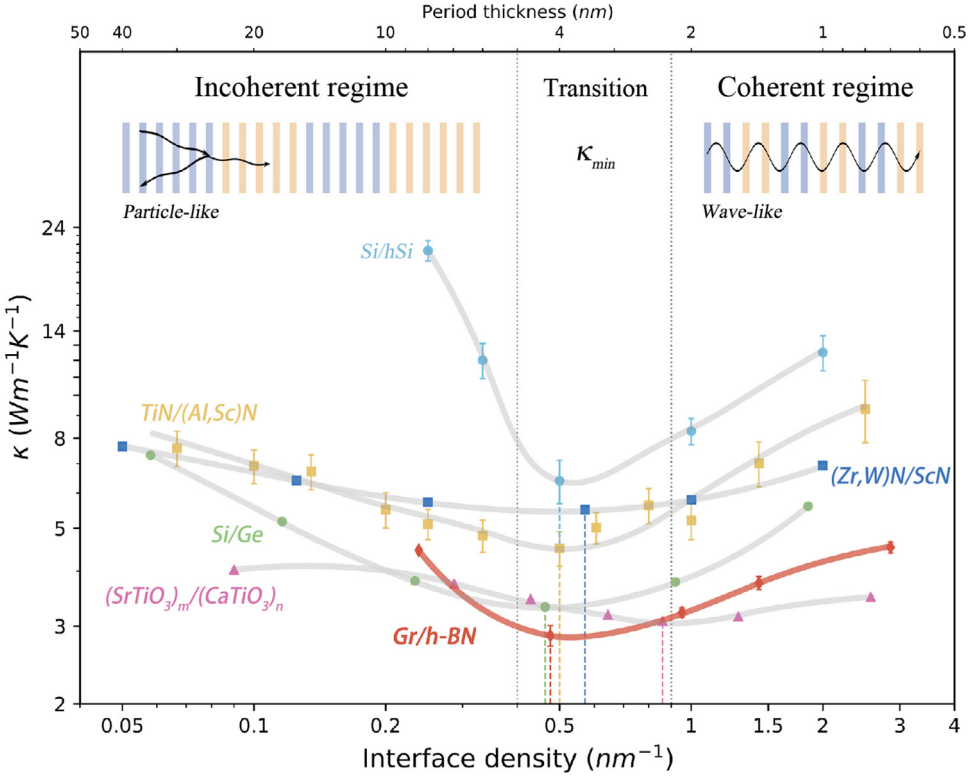

Fig. 7. The out-of-plane thermal conductivity of some typical vdW superlattices as a function of interfacial density at 300K. These include (Zr,W)N/ScN [14] and TiN/(Al,Sc)N [15], which are metal/semiconductor superlattices, the chalcogenide superlattice $(SrTiO_3)_m/(CaTiO_3)_n$ [16], the Si-dominated superlattice Si/hSi (heavy silicon) [6], and the nanowire superlattice Si/Ge [20], as well as Gr/h-BN in this study. The inset depicts a schematic diagram of phonon thermal transport, which consists of three parts divided by interface density: the coherent regime, the incoherent regime, and the transition regime between the former two where there exists a thermal conductivity minimum. The vertical dashed lines in the transition regime correspond to the locations where the six superlattice thermal conductivity minimum occur.

the fact that the phonon MFP of SL_1 in the incoherent transport regime is similar to that of SL_2 but the thermal conductivity is substantially higher. In addition, from the decomposition of the phonon MFP in the frequency domain in Fig. 6(d), the improvement of the phonon MFP within the coherent transport regime is mainly concentrated in the low-frequency band of $0 \sim 4THz$, which is also consistent with the results of $\kappa(\omega)$.

3.2.2. Effect of temperature

Temperature effects, which are intimately connected to thermal issues, are a necessary and unavoidable factor in the analysis of thermal transport problems. It is not only useful for determining the required thermal properties in various hotspot application scenarios, but also has considerable potential for deeper performance modulation. To this end, the following series of studies have been carried out to investigate temperature effects in the Gr/h-BN vdW superlattice.

To begin, the out-of-plane thermal conductivities of five Gr/h-BN vdW superlattices $SL_1 \sim SL_5$ were calculated at four different temperatures of 100K, 200K, 300K, and 500K, and the results are plotted in Fig. 8(a). At 200K, 300K, and 500K, the thermal conductivity all show a tantamount decreasing and then increasing trend with increasing interface density, and all three regimes of phonon transport are distinctly recognizable. At the temperature down to 100K, however, the thermal conductivity tends to be curbed monotonically with increasing interfacial density, and its value is nearly an order of magnitude higher than that at other temperatures. In order to clarify the reason for this discrepancy, the phonon MFP versus interface density at 100K and 300K is compared in Fig. 8(c). Very significantly, the phonon MFP of the Gr/h-BN vdW superlattice at 100K is, on the whole, much higher than that at 300K. Specifically, the former is about 10 to 20 times higher than the latter. With such a high phonon MFP, almost two orders of magnitude thicker than the superlattice period thickness, the phonon transport will be almost entirely in a wave-like coherent transport regime, so that changes in the interface density will have little effect on the out-of-plane thermal conductivity contributed by the phonon coherent transport. Therefore, the phonon scattering that occurs at the hetero-interfaces will be the main factor affecting the thermal conductivity, which explains the monotonically decreasing trend of the thermal conductivity with increasing interface density.

Following that, the Gr/h-BN vdW superlattices SL_2, SL_4, and SL_5 were chosen as representative structures and their respective out-of-plane thermal conductivities were calculated at temperatures ranging from 300K to 500K with an interval of 50K to investigate the specific effects of temperature fluctuations on the out-of-plane thermal conductivity within the possible application hotspot temperature range. It can be clearly observed from Fig. 8(b) that the thermal conductivity tends to impair approximately linearly with increasing temperature, due to the enhanced anharmonic phonon (Umklapp) scattering at high temperatures. Further, the three superlattices SL_2, SL_4, and SL_5 are exposed to Umklapp scattering rates of around 4.60×10^{-3}, 7.86×10^{-3}, and 9.71×10^{-3}, respectively, in $Wm^{-1}K^{-2}$, which are calculated by taking the absolute value of the slope of the linear fit results obtained. Because the phonon scattering from this superlattice occurs mostly at the Gr/h-BN hetero-interfaces, the Umklapp scattering rate is steadily increased as the interface density increases. From the results of Fig. 8(d) for the out-of-plane thermal conductivity of superlattice SL_5 at 300K, 400K, and 500K, it can be seen that an increase in temperature will weaken the peak of $\kappa(\omega)$ and thus reduce the thermal conductivity without changing its overall shape. This prop-

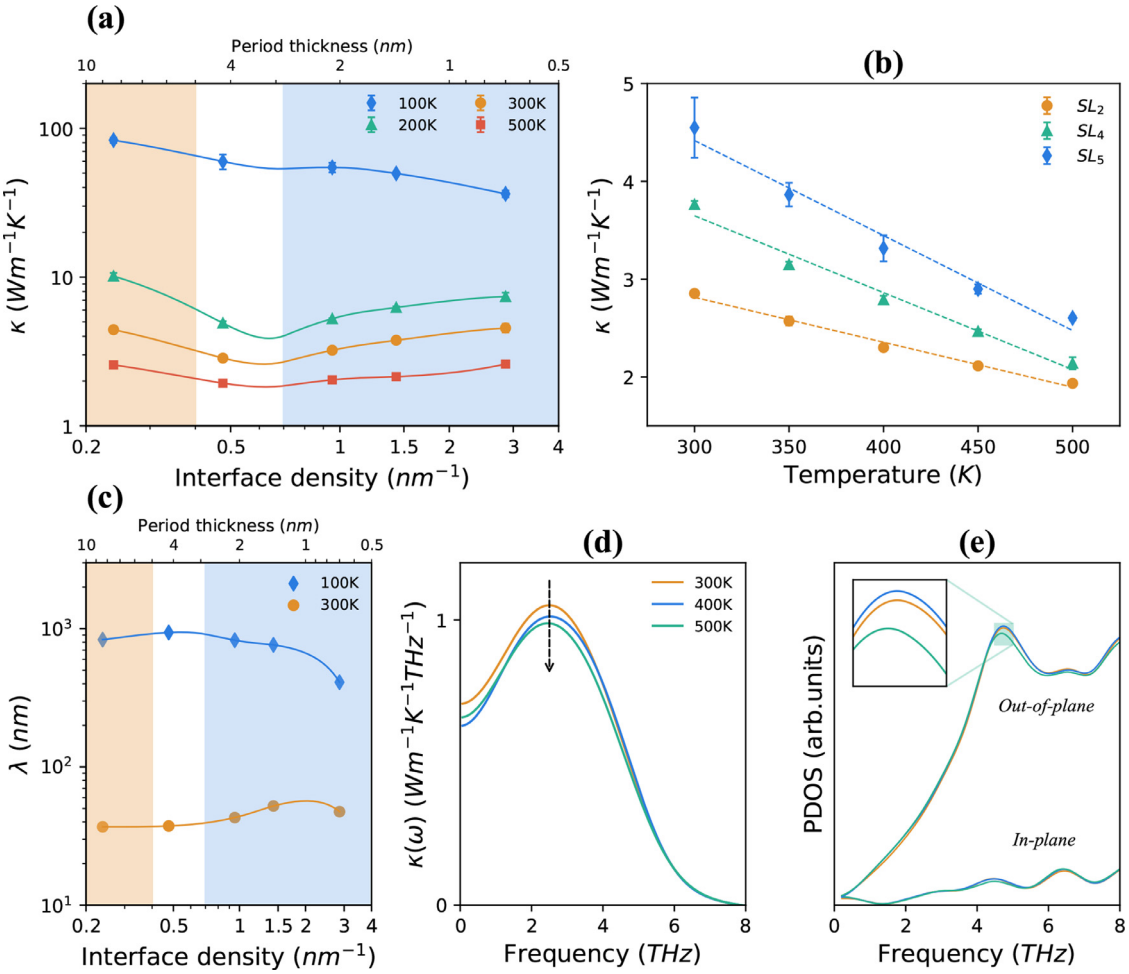

Fig. 8. (a) Relationship between out-of-plane thermal conductivity and interfacial density of Gr/h-BN vdW superlattices at four temperatures: 100K, 200K, 300K, and 500K. (b) Variation of out-of-plane thermal conductivity with temperature for Gr/h-BN vdW superlattices SL_2, SL_4, and SL_5, where the dashed lines show the results of a linear fit to the corresponding data. (c) The phonon MFP versus interface density for the Gr/h-BN vdW superlattice SL_5 at 100K and 300K. (d) Spectral out-of-plane thermal conductivity $\kappa(\omega)$, (e) in-plane and out-of-plane PDOS as a function of phonon frequency for Gr/h-BN vdW superlattices SL_5 at 300K, 400K, and 500K. The inset in (e) is an illustration of the amplification of the out-of-plane PDOS in the low-frequency peak region where the three curves differ significantly. Note that the colored background divisions in (a) and (c) correspond to the three regimes of phonon transport in the same sense as in Fig. 6(a).

erty has a similar spectral thermal conductivity behavior to the result of increased phonon scattering due to increased interfacial density in the non-coherent transport regime of Fig. 6(c), which is another indication of the homology between the two in terms of decreased thermal conductivity due to increased phonon scattering. Specifically, further analysis is carried out by means of phonon density of states (PDOS) results that capture the phonon activity of the material in different modes as follows:

$$PDOS_{i\alpha}(\omega) = \int_{-\infty}^{+\infty} \langle v_{i\alpha}(t) v_{i\alpha}(0) \rangle e^{-2\pi i \omega t} dt \quad (\alpha = x, y, z) \tag{22}$$

where $\langle v_{i\alpha}(t) v_{i\alpha}(0) \rangle$ refers to the velocity auto-correlation function (VACF) for atom i in the α-direction at the related time t, which is similar to the virial-velocity correlation function in Eq. (10). In this study, the in-plane PDOS is represented by the average of the results in the x and y directions, and the out-of-plane PDOS is represented by the results in the z direction. In Fig. 8(e), the results of the superlattice SL_5 are plotted at 300K, 400K, and 500K for the in-plane PDOS in the low-frequency band, where it can be seen that the out-of-plane PDOS is dominant and the high temperature shows a significant weakening effect on the low-frequency peak.

3.2.3. Effect of interface coupling strength χ

In the Gr/h-BN vdW superlattice in this study, the key parameter of interfacial coupling strength (χ), as defined in Eq. (15), which determines the strength of the interlayer vdW interaction in its multilayer structure, will undoubtedly have a significant impact on its out-of-plane thermal conductivity. The out-of-plane thermal conductivities of Gr/h-BN vdW superlattices with different interfacial densities at χ of 0.5, 1.0, and 2.0 were firstly calculated at 300K and plotted in Fig. 9(a). Laterally, with the change in interface density, the trends in thermal conductivity exhibited for different cases of χ are approximately the same, and the three regimes of phonon transport are clearly delineated. In the longitudinal direction, the increase in the χ has a significant enhancement effect on the out-of-plane thermal conductivity of the superlattice, which is achieved by raising the phonon coupling degree at the vdW interface to improve the phonon thermal transport capacity. In order to quantify the enhancement of thermal conductivity brought about by χ, Gr/h-BN vdW superlattices SL_2, SL_4, and SL_5 are selected as representative structures, and their out-of-plane thermal conductivity is plotted with χ in Fig. 9(b). After a linear fit, the out-of-plane thermal conductivity of the three superlattices SL_2, SL_4, and SL_5 are about 4.58, 6.15 and 7.37 with χ, respectively, demonstrating that the higher the interfacial density, the greater the increase in thermal conductivity with rising χ. The higher interface

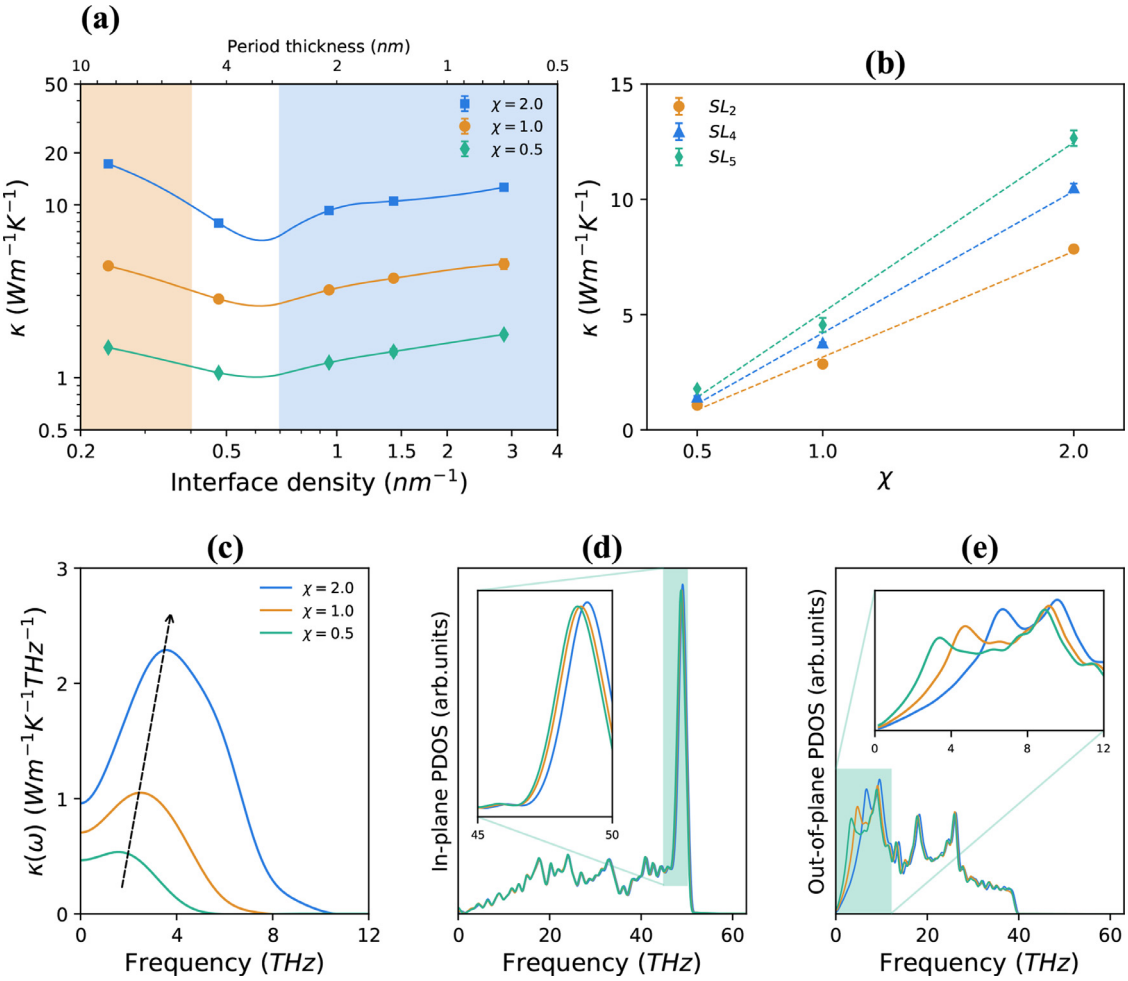

Fig. 9. (a) The out-of-plane thermal conductivity of the Gr/h-BN vdW superlattice as a function of the interfacial density at 300K for interfacial coupling strengths χ of 0.5, 1.0, and 2.0, respectively. (b) Variation of out-of-plane thermal conductivity with χ for Gr/h-BN vdW superlattices SL_2, SL_4, and SL_5, where the dashed lines show the results of a linear fit to the corresponding data. Relationships between (c) spectral out-of-plane thermal conductivity $\kappa(\omega)$, (d) in-plane PDOS, and (e) out-of-plane PDOS with the phonon frequency for Gr/h-BN vdW superlattices SL_5 at different χ. The dashed arrows in (c) indicate the approximate trend of the location of the peaks. The insets in (d) and (e) show enlarged diagrams at the respective characteristic peaks. Notably, for transverse comparison purposes, the (d) and (e) have exactly the same value domain.

density means that the density of the Gr/h-BN hetero-interfaces with relatively high thermal resistance is higher, which means that the weakening effect on thermal conductivity caused by phonon-phonon scattering at the interface is stronger, in the same way as the results exhibited by the random superlattice in Fig. 6(a). In this case, the increase in χ compensates for this weakening effect to some extent in terms of improving the thermal transport capacity of the interfacial phonons. As a result, superlattices with higher interfacial densities are subject to more significant compensatory effects in the case of increased χ, which in turn manifests itself in higher thermal conductivity gains.

Further, the spectral out-of-plane thermal conductivity of the superlattice SL_5 was calculated for different χ, as shown in Fig. 9(c). As a whole, the difference between the phonon dynamics of $\kappa(\omega)$ at different χ while all concentrated in the low-frequency region of less than $12THz$ is significant. Specifically, as χ rises, the characteristic peak of $\kappa(\omega)$ gradually moves towards the higher frequency band up within $8THz$ while exhibiting a significant broadening and a significant increase in the peak. This means that the increase in χ not only improves the ability to thermal transport phonons in the current frequency range, but also allows new low-frequency phonons in a wider frequency range to be involved in the transport process. In order to be able to capture the phonon dynamics information more visually, the in-plane and out-of-plane PDOS results corresponding to the three cases in Fig. 9(c) are also plotted in Figs. 9(d-e), respectively. It can be seen that out-of-plane phonons are still absolutely dominant in the low-frequency region where they contribute almost entirely to the out-of-plane thermal conductivity, and as χ increases the low-frequency peaks of out-of-plane PDOS exhibit a peak increase and shift towards higher frequencies. For in-plane PDOS, however, the effect of χ is mainly at the high-frequency peak around $48THz$, and to a much lesser extent than that suffered by out-of-plane PDOS.

4. Conclusion

In summary, the extensive MD simulations including non-equilibrium, homogeneous non-equilibrium and their respective spectral decomposition as well as a phonon level mechanistic analysis were executed to investigate and dissect the out-of-plane phonon thermal transport behavior of the Gr/h-BN vdW superlattice. It is found that as the interface density increases, the superlattice exhibits a transition from the incoherent to coherent phonon transport regimes along the out-of-plane direction, with a minimum thermal conductivity at the junction of the two. In the non-coherent transport regime, the increase in scattering rate at the Gr/h-BN hetero-interfaces caused by the increased interfacial den-

sity is the underlying cause of the decrease in out-of-plane thermal conductivity, which reflects the particle-like phonon transport properties. However, as the interface density increases further, the increase in the phonon MFP allows the phonon transport of the superlattice to take on a wave-like nature and enter the coherent transport regime with an incessant increase in thermal conductivity. This process can be attributed to a game between heterointerfaces phonon scattering and coherent transport effects, which have opposite effects on the out-of-plane thermal conductivity of the superlattice. In addition, the above-mentioned properties of phonon thermal transport of the Gr/h-BN vdW superlattice were also discussed as influenced by temperature and interfacial coupling strength. These findings provide a new understanding of the phonon thermal transport mechanism in Gr/h-BN vdW superlattices, which is expected to further advance the development of superlattice nanodevices for optimal thermal management and thermal design.

Declaration of Competing Interest

The authors declared that they have no conflicts of interest to this work. We also declare that we do not have any commercial or associative interest that represents a conflict of interest in connection with the work submitted.

CRediT authorship contribution statement

Xin Wu: Conceptualization, Methodology, Software, Validation, Formal analysis, Investigation, Writing – original draft, Writing – review & editing, Visualization. **Qiang Han:** Resources, Supervision, Project administration, Funding acquisition.

Acknowledgments

The authors are grateful for support from the National Natural Science Foundation of China (11972160), Guangdong Basic and Applied Basic Research Foundation (2019A1515011900), Science and Technology Program of Guangzhou, China (202002030367).

Supplementary material

Supplementary material associated with this article can be found, in the online version, at doi:10.1016/j.ijheatmasstransfer.2021.122390.

References

[1] I.K. Schuller, New class of layered materials, Phys. Rev. Lett. 44 (1980) 1597–1600, doi:10.1103/PhysRevLett.44.1597.
[2] M. Maldovan, Phonon wave interference and thermal bandgap materials, Nat. Mater. 14 (2015) 669–674, doi:10.1103/PhysRevLett.44.1597.
[3] W. Ouyang, O. Hod, M. Urbakh, Parity-dependent moire superlattices in graphene=h-BN heterostructures: A Route to mechanomutable metamaterials, Phys. Rev. Lett. 126 (2021) 216101, doi:10.1103/PhysRevLett.126.216101.
[4] M.V. Simkin, G.D. Mahan, Minimum thermal conductivity of superlattices, Phys. Rev. Lett. 84 (2000) 927–930, doi:10.1103/PhysRevLett.84.927.
[5] B. Yang, G. Chen, Partially coherent phonon heat conduction in superlattices, Phys. Rev. B 67 (2003) 195311, doi:10.1103/PhysRevB.67.195311.
[6] B. Latour, S. Volz, Y. Chalopin, Microscopic description of thermal-phonon coherence: from coherent transport to diffuse interface scattering in superlattices, Phys. Rev. B 90 (2014) 014307, doi:10.1103/PhysRevB.90.014307.
[7] R. Hu, S. Iwamoto, L. Feng, S. Ju, S. Hu, M. Ohnishi, N. Nagai, K. Hirakawa, J. Shiomi, Machine-Learning-Optimized aperiodic superlattice minimizes coherent phonon heat conduction, Phys. Rev. X 10 (2020) 021050, doi:10.1103/PhysRevX.10.021050.
[8] Q.D. Gibson, T. Zhao, L.M. Daniels, H.C. Walker, R. Daou, S. Hbert, M. Zanella, M.S. Dyer, J.B. Claridge, B. Slater, M.W. Gaultois, F. Cor, J. Alaria, M.J. Rosseinsky, Low thermal conductivity in a modular inorganic material with bonding anisotropy and mismatch, Science 373 (2021) 1017–1022, doi:10.1126/science.abh1619.
[9] X.-K. Chen, K.-Q. Chen, Thermal transport of carbon nanomaterials, J. Phys.: Condens. Matter 32 (2020) 153002, doi:10.1088/1361-648X/ab5e57.
[10] X.-K. Chen, X.-Y. Hu, P. Jia, Z.-X. Xie, J. Liu, Tunable anisotropic thermal transport in porous carbon foams: the role of phonon coupling, Int. J. Mech. Sci. 206 (2021) 106576, doi:10.1016/j.ijmecsci.2021.106576.
[11] Z. Zhang, Y. Guo, M. Bescond, J. Chen, M. Nomura, S. Volz, Coherent thermal transport in nano-phononic crystals: an overview, APL Mater. 9 (2021) 081102, doi:10.1063/5.0059024.
[12] M.N. Luckyanova, J. Garg, K. Esfarjani, A. Jandl, M.T. Bulsara, A.J. Schmidt, A.J. Minnich, S. Chen, M.S. Dresselhaus, Z. Ren, E.A. Fitzgerald, G. Chen, Coherent phonon heat conduction in superlattices, Science 338 (2012) 936–939, doi:10.1126/science.1225549.
[13] S. Chakraborty, C.A. Kleint, A. Heinrich, C.M. Schneider, J. Schumann, M. Falke, S. Teichert, Thermal conductivity in strain symmetrized Si/Ge superlattices on Si(111), Appl. Phys. Lett. 83 (2003) 4184, doi:10.1063/1.1628819.
[14] V. Rawat, Y.K. Koh, D.G. Cahill, T.D. Sands, Thermal conductivity of (Zr,W)N/ScN metal/ semiconductor multilayers and superlattices, J. Appl. Phys. 105 (2009) 024909, doi:10.1063/1.3065092.
[15] B. Saha, Y.R. Koh, J.P. Feser, S. Sadasivam, T.S. Fisher, A. Shakouri, T.D. Sands, Phonon wave effects in the thermal transport of epitaxial TiN/(Al,Sc)N metal/ semiconductor superlattices, J. Appl. Phys. 121 (2017) 015109, doi:10.1063/1.4973681.
[16] J. Ravichandran, A.K. Yadav, R. Cheaito, P.B. Rossen, A. Soukiassian, S.J. Suresha, J.C. Duda, B.M. Foley, C.-H. Lee, Y. Zhu, A. Lichtenberger, J.E. Moore, D.A. Muller, D.G. Schlom, P.E. Hopkins, A. Majumdar, R. Ramesh, M.A. Zurbuchen, Crossover from incoherent to coherent phonon scattering in epitaxial oxide superlattices, Nat. Mater. 13 (2014) 168–172, doi:10.1038/nmat3826.
[17] H. Kwon, A.I. Khan, C. Perez, M. Asheghi, E. Pop, K.E. Goodson, Uncovering thermal and electrical properties of Sb_2Te_3/GeTe superlattice films, Nano Lett. 21 (2021) 5984–5990, doi:10.1021/acs.nanolett.1c00947.
[18] F. Momeni, B. Mehrafrooz, A. Montazeri, A. Rajabpour, MD-based design of bilayer graphene-hBNheterostructures: an insight into enhanced thermal transport, Int. J. Heat Mass Transf. 150 (2020) 119282, doi:10.1016/j.ijheatmasstransfer.2019.119282.
[19] M.S. Alborzi, A. Rajabpour, Thermal transport in van der Waals graphene/boron-nitride structure: a molecular dynamics study, Eur. Phys. J. Plus 136 (2021) 959, doi:10.1140/epjp/s13360-021-01901-2.
[20] M. Hu, D. Poulikakos, Si/Ge superlattice nanowires with ultralow thermal conductivity, Nano Lett. 12 (2012) 5487–5494, doi:10.1021/nl301971k.
[21] X.-K. Chen, M. Pang, T. Chen, D. Du, K.-Q. Chen, Thermal rectification in asymmetric graphene/hexagonal boron nitride van der waals heterostructures, ACS Appl. Mater. Interfaces 12 (2020) 15517—15526, doi:10.1021/acsami.9b22498.
[22] S. Hu, Z. Zhang, P. Jiang, J. Chen, S. Volz, M. Nomura, B. Li, Randomness-Induced phonon localization in graphene heat conduction, J. Phys. Chem. Lett. 9 (2018) 3959–3968, doi:10.1021/acs.jpclett.8b01653.
[23] I.M. Felix, L.F.C. Pereira, Suppression of coherent thermal transport in quasiperiodic graphene-hBN superlattice ribbons, Carbon N Y 160 (2020) 335–341, doi:10.1016/j.carbon.2019.12.090.
[24] M. An, D. Chen, W. Ma, S. Hu, X. Zhang, Directly visualizing the crossover from incoherent to coherent phonons in two-dimensional periodic $MoS_2/MoSe_2$ arrayed heterostructure, Int. J. Heat Mass Transf. 178 (2021) 121630, doi:10.1016/j.ijheatmasstransfer.2021.121630.
[25] L. Razzaghi, F. Khoeini, A. Rajabpour, M. Khalkhali, Thermal transport in two-dimensional C_3N/C_2N superlattices: a molecular dynamics approach, Int. J. Heat Mass Transf. 177 (2021) 121561, doi:10.1016/j.ijheatmasstransfer.2021.121561.
[26] B. Jiang, S. Wang, J. Sun, Z. Liu, Controllable synthesis of wafer-scale graphene films: challenges, status, and perspectives, Small (2021) 2008017, doi:10.1002/smll.202008017.
[27] S.-J. Liang, B. Cheng, X. Cui, F. Miao, Van der waals heterostructures for high-Performance device applications: challenges and opportunities, Adv. Mater. 32 (2019) 1903800, doi:10.1002/adma.201903800.
[28] B. Zhao, Z. Wan, Y. Liu, J. Xu, X. Yang, D. Shen, Z. Zhang, C. Guo, Q. Qian, J. Li, R. Wu, Z. Lin, X. Yan, B. Li, Z. Zhang, H. Ma, B. Li, X. Chen, Y. Qiao, I. Shakir, Z. Almutairi, F. Wei, Y. Zhang, X. Pan, Y. Huang, Y. Ping, X. Duan, X. Duan, High-order superlattices by rolling up van der waals heterostructures, Nature 591 (2021) 385–390, doi:10.1038/s41586-021-03338-0.
[29] T. Iwasaki, Y. Morita, S. Nakaharai, Y. Wakayama, E. Watanabe, D. Tsuya, K. Watanabe, T. Taniguchi, S. Moriyama, Fabrication of folded bilayer-bilayer graphene/hexagonal boron nitride superlattices, Appl. Phys. Express 13 (2020) 035003, doi:10.35848/1882-0786/ab790d.
[30] X. Wu, Q. Han, Phonon thermal transport across multilayer graphene/hexagonal boron nitride van der waals heterostructures, ACS Appl. Mater. Interfaces 13 (2021) 32564–32578, doi:10.1021/acsami.1c08275.
[31] F. Mller-Plathe, A simple nonequilibrium molecular dynamics method for calculating the thermal conductivity, J. Chem. Phys. 106 (1997) 6082, doi:10.1063/1.473271.
[32] J. CHEN, G. ZHANG, L.I. Baowen, Molecular dynamics simulations of heat conduction in nanostructures: effect of heat bath, J. Phys. Soc. Jpn. 79 (2010) 074604, doi:10.1143/JPSJ.79.074604.
[33] Z. Li, S. Xiong, C. Sievers, Y. Hu, Z. Fan, N. Wei, H. Bao, S. Chen, D. Donadio, T. Ala-Nissila, Influence of thermostatting on nonequilibrium molecular dynamics simulations of heat conduction in solids, J. Chem. Phys. 151 (2019) 234105, doi:10.1063/1.5132543.
[34] D.J. EVANS, Homogeneous NEMD algorithm for thermal conductivity—Application of non-canonical linear response theory, Phys. Lett. 91A (1982) 457–460, doi:10.1016/0375-9601(82)90748-4.

[35] Z. Fan, H. Dong, A. Harju, T. Ala-Nissila, Homogeneous nonequilibrium molecular dynamics method for heat transport and spectral decomposition with many-body potentials, Phys. Rev. B 99 (2019) 064308, doi:10.1103/PhysRevB.99.064308.
[36] M.S. Green, Markoff random processes and the statistical mechanics of time-Dependent phenomena. II. irreversible processes in fluids, J. Chem. Phys. 22 (1954) 398–413, doi:10.1063/1.1740082.
[37] R. Kubo, Statistical-mechanical theory of irreversible processes. i. general theory and simple applications to magnetic and conduction problems, J. Phys. Soc. Jpn. 12 (1957) 570–586, doi:10.1143/JPSJ.12.570.
[38] K. Saaskilahti, J. Oksanen, J. Tulkki, S. Volz, Role of anharmonic phonon scattering in the spectrally decomposed thermal conductance at planar interfaces, Phys. Rev. B 90 (2014) 134312, doi:10.1103/PhysRevB.90.134312.
[39] K. Saaskilahti, J. Oksanen, S. Volz, J. Tulkki, Frequency-dependent phonon mean free path in carbon nanotubes from nonequilibrium molecular dynamics, Phys. Rev. B 91 (2015) 115426, doi:10.1103/PhysRevB.91.115426.
[40] Z. Fan, L.F.C. Pereira, P. Hirvonen, M.M. Ervasti, K.R. Elder, D. Donadio, T. Ala-Nissila, A. Harju, Thermal conductivity decomposition in two-dimensional materials: application to graphene, Phys. Rev. B 95 (2017) 144309, doi:10.1103/PhysRevB.95.144309.
[41] Z. Fan, L.F.C. Pereira, H.-Q. Wang, J.-C. Zheng, D. Donadio, A. Harju, Force and heat current formulas for many-body potentials in molecular dynamics simulations with applications to thermal conductivity calculations, Phys. Rev. B 92 (2015) 094301, doi:10.1103/PhysRevB.92.094301.
[42] Z. Fan, W. Chen, V. Vierimaa, A. Harju, Efficient molecular dynamics simulations with many-body potentials on graphics processing units, Comput. Phys. Commun. 218 (2017) 10–16, doi:10.1016/j.cpc.2017.05.003.
[43] D. Surblys, H. Matsubara, G. Kikugawa, T. Ohara, Application of atomic stress to compute heat flux via molecular dynamics for systems with many-body interactions, Phys. Rev. E 99 (2019) 051301(R), doi:10.1103/PhysRevE.99.051301.
[44] A. Knac, J.B. Haskins, C. Sevik, T. Cagn, Thermal conductivity of BN-C nanostructures, Phys. Rev. B 86 (2012) 115410, doi:10.1103/PhysRevB.86.115410.
[45] A.K. Rapp, C.J. Casewit, K.S. Colwell, W.A. Goddard III, W.M. Skif, UFF, a full periodic table force field for molecular mechanics and molecular dynamics simulations, J. Am. Chem. Soc. 114 (1992) 10024–10035, doi:10.1021/ja00051a040.
[46] P.K. Schelling, S.R. Phillpot, P. Keblinski, Comparison of atomic-level simulation methods for computing thermal conductivity, Phys. Rev. B 65 (2002) 144306, doi:10.1103/PhysRevB.65.144306.
[47] X. Gu, Z. Fan, H. Bao, C.Y. Zhao, Revisiting phonon-phonon scattering in single-layer graphene, Phys. Rev. B 100 (2019) 064306, doi:10.1103/PhysRevB.100.064306.
[48] K. Azizi, P. Hirvonen, Z. Fan, A. Harju, K.R. Elder, T. Ala-Nissila, S.M.V. Allaei, Kapitza thermal resistance across individual grain boundaries in graphene, Carbon N Y 125 (2017) 384–390, doi:10.1016/j.carbon.2017.09.059.
[49] Y. Wang, H. Huang, X. Ruan, Decomposition of coherent and incoherent phonon conduction in superlattices and random multilayers, Phys. Rev. B 90 (2014) 165406, doi:10.1103/PhysRevB.90.165406.